A&A 658, A91 (2022)
https://doi.org/10.1051/0004-6361/202142369

Astronomy & Astrophysics

Photo-astrometric distances, extinctions, and astrophysical parameters for *Gaia* EDR3 stars brighter than $G = 18.5$★

F. Anders[1,2], A. Khalatyan[2], A. B. A. Queiroz[2,3,4], C. Chiappini[2,3], J. Ardèvol[1], L. Casamiquela[5], F. Figueras[1], Ó. Jiménez-Arranz[1], C. Jordi[1], M. Monguió[1], M. Romero-Gómez[1], D. Altamirano[1], T. Antoja[1], R. Assaad[6], T. Cantat-Gaudin[7], A. Castro-Ginard[8], H. Enke[2], L. Girardi[9], G. Guiglion[2], S. Khan[10], X. Luri[1], A. Miglio[11,12,13], I. Minchev[2], P. Ramos[14], B. X. Santiago[15,3], and M. Steinmetz[2]

[1] Institut de Ciències del Cosmos, Universitat de Barcelona (IEEC-UB), Martí i Franquès 1, 08028 Barcelona, Spain
e-mail: fanders@icc.ub.edu
[2] Leibniz-Institut für Astrophysik Potsdam (AIP), An der Sternwarte 16, 14482 Potsdam, Germany
e-mail: akhalatyan@aip.de
[3] Laboratório Interinstitucional de e-Astronomia – LIneA, Rua Gal. José Cristino 77, Rio de Janeiro 20921-400, Brazil
[4] Institut für Physik und Astronomie, Universität Potsdam, Haus 28 Karl-Liebknecht-Str. 24/25, 14476 Golm, Germany
[5] Laboratoire d'Astrophysique de Bordeaux, Univ. Bordeaux, CNRS, B18N, allée Geoffroy Saint-Hilaire, 33615 Pessac, France
[6] Department of Physics, University of Surrey, Guildford GU2 7XH, UK
[7] Max-Planck-Institut für Astronomie, Königstuhl 17, 69117 Heidelberg, Germany
[8] Leiden Observatory, Leiden University, Niels Bohrweg 2, 2333 CA Leiden, The Netherlands
[9] Osservatorio Astronomico di Padova, INAF, Vicolo dell'Osservatorio 5, 35122 Padova, Italy
[10] Institute of Physics, Laboratory of Astrophysics, École Polytechnique Fédérale de Lausanne (EPFL), Observatoire de Sauverny, 1290 Versoix, Switzerland
[11] Dipartimento di Fisica e Astronomia, Università di Bologna, Via Gobetti 93/2, 40129 Bologna, Italy
[12] INAF – Osservatorio di Astrofisica e Scienza dello Spazio di Bologna, Via Gobetti 93/3, 40129 Bologna, Italy
[13] School of Physics and Astronomy, University of Birmingham, Edgbaston B15 2TT, UK
[14] Observatoire astronomique de Strasbourg, Université de Strasbourg, CNRS, 11 rue de l'Université, 67000 Strasbourg, France
[15] Instituto de Física, Universidade Federal do Rio Grande do Sul, Caixa Postal 15051, Porto Alegre 91501-970, Brazil

Received 4 October 2021 / Accepted 5 November 2021

ABSTRACT

We present a catalogue of 362 million stellar parameters, distances, and extinctions derived from *Gaia*'s Early Data Release (EDR3) cross-matched with the photometric catalogues of Pan-STARRS1, SkyMapper, 2MASS, and AllWISE. The higher precision of the *Gaia* EDR3 data, combined with the broad wavelength coverage of the additional photometric surveys and the new stellar-density priors of the `StarHorse` code, allows us to substantially improve the accuracy and precision over previous photo-astrometric stellar-parameter estimates. At magnitude $G = 14$ (17), our typical precisions amount to 3% (15%) in distance, 0.13 mag (0.15 mag) in V-band extinction, and 140 K (180 K) in effective temperature. Our results are validated by comparisons with open clusters, as well as with asteroseismic and spectroscopic measurements, indicating systematic errors smaller than the nominal uncertainties for the vast majority of objects. We also provide distance- and extinction-corrected colour-magnitude diagrams, extinction maps, and extensive stellar density maps that reveal detailed substructures in the Milky Way and beyond. The new density maps now probe a much greater volume, extending to regions beyond the Galactic bar and to Local Group galaxies, with a larger total number density. We publish our results through an ADQL query interface (`gaia.aip.de`) as well as via tables containing approximations of the full posterior distributions. Our multi-wavelength approach and the deep magnitude limit render our results useful also beyond the next *Gaia* release, DR3.

Key words. stars: distances – stars: fundamental parameters – Galaxy: general – Galaxy: stellar content – Galaxy: structure

1. Introduction

Since its launch in 2013 the European Space Agency's flagship mission *Gaia* (Gaia Collaboration 2016) has revolutionised Galactic astronomy and its neighbouring fields (Brown 2021). The precision and accuracy of our knowledge of the Solar System (e.g. Gaia Collaboration 2018a; Bailer-Jones et al. 2018a; Portegies Zwart 2021), stellar astrophysics (e.g. Jao et al. 2018; Lanzafame et al. 2019; Mowlavi et al. 2021), the immediate solar vicinity (e.g. Gaia Collaboration 2021a,b; Reylé et al. 2021), open star clusters (e.g. Cantat-Gaudin et al. 2018; Cantat-Gaudin & Anders 2020; Castro-Ginard et al. 2020), distant regions of the Milky Way (e.g. Ramos et al. 2021; Gaia Collaboration 2021c; Zari et al. 2021) and the Local Group (e.g. Gaia Collaboration 2018b, 2021d; Antoja et al. 2020), the Galactic potential (e.g. Crosta et al. 2020; Cunningham et al. 2020; Hattori et al. 2021), and even the Hubble constant (e.g. Breuval et al. 2020; Riess et al. 2021; Baumgardt & Vasiliev 2021) are constantly increasing thanks to *Gaia*.

In the context of Galactic archaeology, *Gaia* has also enabled a completely new line of precision studies tracing

★ The catalog is available at the CDS via anonymous ftp to `cdsarc.u-strasbg.fr` (`130.79.128.5`) or via `http://cdsarc.u-strasbg.fr/viz-bin/cat/J/A+A/658/A91`

the past accretion events of the Milky Way (Helmi 2020; Kruijssen et al. 2020; Pfeffer et al. 2021). Often this is achieved by combining the complete phase-space information with detailed chemistry from spectroscopic surveys (e.g. Aguado et al. 2021; Gudin et al. 2021; Limberg et al. 2021a,b; Montalbán et al. 2021; Naidu et al. 2021; Shank et al. 2021).

The latest *Gaia* data release, Early Data Release 3 (*Gaia* EDR3; Gaia Collaboration 2021e), covers the first 34 months of observations with positions and photometry for 1.8×10^9 sources (Riello et al. 2021), proper motions and parallaxes for 1.5×10^9 sources (Lindegren et al. 2021a), and radial velocities for 7×10^6 sources (Seabroke et al. 2021; Gaia Collaboration 2021e). With respect to Data Release 2 (*Gaia* DR2; Gaia Collaboration 2018c), the proper motions are by a factor of 2 more precise, and parallax uncertainties are reduced by 20% (see Fabricius et al. 2021 for details).

In a previous work (Anders et al. 2019, hereafter A19) based on *Gaia* DR2, our group derived Bayesian stellar parameters, distances, and extinctions for 265 million stars brighter than $G = 18$ with the `StarHorse` code (Santiago et al. 2016; Queiroz et al. 2018). The combination of precise *Gaia* DR2 parallaxes and optical photometry with the multi-wavelength photometry of Pan-STARRS1 (Chambers et al. 2016), 2MASS (Cutri et al. 2003), and AllWISE (Cutri et al. 2013) substantially improved the accuracy of the extinction and effective temperature estimates provided with only *Gaia* DR2 (Andrae et al. 2018). A selection of the most reliable in- and output data, a sample of 137 million stars, allowed A19 to detect the imprint of the Galactic bar both in the stellar density distribution and in proper motion maps (further studied with APOGEE spectroscopy in Queiroz et al. 2021).

The results of our *Gaia* DR2 `StarHorse` run presented in A19 have been used in a wide variety of science cases, including exoplanetary research (Sozzetti et al. 2021), interstellar extinction (Leike et al. 2020), runaway stars from supernova remnants (Lux et al. 2021), X-ray transients (Lamer et al. 2021), γ-ray astronomy (Steppa & Egberts 2020), ,the Galactic escape speed curve (Monari et al. 2018), the three-dimensionl phase-space structure of the Milky Way disc (Carrillo et al. 2019), and spectroscopic survey simulations (Chiappini et al. 2019).

Anticipating a significant improvement thanks to the new *Gaia* data, we update our analysis using the new EDR3 data in this paper, addressing some of the known caveats of our previous data release and reducing the uncertainties of the main output parameters by a factor of 2. In a parallel effort we will be publishing `StarHorse` results for spectroscopic surveys combined with *Gaia* (≈6 million stars) in Queiroz et al. (in prep.).

This paper is structured as follows: Section 2 presents the input data and Sect. 3 our method. In particular, Sect. 3.1 describes the updates to our code with respect to previous applications, and Sect. 3.3 explains how we flagged the new `StarHorse` results for *Gaia* EDR3. We then present some first astrophysical results in Sect. 4, mainly focussing on colour-magnitude diagrams (CMDs), extinction maps, and stellar density maps. The stellar density maps demonstrate the emergence of substructure beyond the detection of the Galactic bar, for example when focussing on metal-poor stars, the Magellanic Clouds, or the outer Milky Way halo. The precision and accuracy of the `StarHorse` EDR3 parameters are discussed in Sect. 5, providing comparisons to Galactic open clusters (OCs Cantat-Gaudin et al. 2020; Dias et al. 2021), asteroseismically derived parameters for giant stars (Miglio et al. 2021), and spectroscopic stellar parameters from the GALAH survey (Buder et al. 2021). We also make comparisons to previous results obtained from *Gaia* DR2 and EDR3 in Sect. 6. Finally, we conclude the paper with a summary and a brief outlook to the near future in Sect. 7.

2. Data

As input for `StarHorse`, we use the *Gaia* EDR3 data cross-matched with 2MASS, AllWISE, Pan-STARRS1, and SkyMapper (Onken et al. 2019), in the sense that all available good photometric measurements are used in the inference. The calibrations used in this paper are summarised in Table 1.

From *Gaia* EDR3 we use the parallaxes and three-band photometry, together with their associated uncertainties. We recalibrate the parallaxes following the recommendations of Lindegren et al. (2021b) who assessed the variations in the parallax zero point as a function of sky position, magnitude, and colour[1]. Furthermore, we inflate the corresponding parallax uncertainties by a magnitude-dependent factor, following Fabricius et al. (2021, see also El-Badry et al. 2021). In particular, we fit the inflation factor to their worst-case scenario of Fig. 19 in Fabricius et al. (2021) (a crowded Large Magellanic Cloud field) to make sure that our parallax uncertainties are not underestimated. A further discussion of the fidelity of the *Gaia* parallaxes in our context is available in Rybizki et al. (2022) and in our Sect. 3.3.1.

Regarding the *Gaia* photometry, we use the precise EDR3 magnitudes (Riello et al. 2021) without any posterior correction other than the G-band correction advertised in Appendix A of Gaia Collaboration (2021e)[2], since they show much lower systematics ($\lesssim$0.01 mag; e.g. Fabricius et al. 2021; Niu et al. 2021) than the previous DR2 photometry (see e.g. Maíz Apellániz & Weiler 2018). For the BP/RP photometry, we follow the recommendation of Fabricius et al. (2021) and do not use magnitudes `phot_bp_mean_mag` > 20.5 or `phot_rp_mean_mag` > 20 in the inference.

The *Gaia* EDR3 cross-match to the large-area photometric surveys 2MASS, AllWISE, Pan-STARRS1 DR1, and SkyMapper DR2 is documented in Marrese et al. (2021). The main novelty with respect to A19 is the inclusion of SkyMapper data. From the SkyMapper DR2 data we only use the *griz* bands (with zero points recalibrated following Huang et al. 2021a) and refrain from using the *u* and *v* bands, because our default extinction law (Schlafly et al. 2016) should not be extrapolated to the ultraviolet.

For Pan-STARRS1, we apply the zero-point corrections recommended by Scolnic et al. (2015), and do not use magnitudes brighter than the saturation limit. With respect to A19, we apply more restrictive filters to the 2MASS and AllWISE photometry: only magnitudes with corresponding photometric quality flags 'A' or 'B' are accepted. The minimum photometric uncertainties used in the inference (reflecting also the systematic uncertainties of the passbands and the bolometric corrections) are given in Table 1. We also note that for $\lesssim$0.5% of the *Gaia* EDR3 sources, the *Gaia* cross-match with 2MASS returns in multiple matches. In these cases (pointing towards possible confusion), we do not use any 2MASS photometry.

[1] Code available at https://gitlab.com/icc-ub/public/gaiadr3_zeropoint/-/tree/master/

[2] https://github.com/agabrown/gaiaedr3-6p-gband-correction/blob/main/GCorrectionCode.ipynb

Table 1. Summary of the calibrations and data curation applied to the astrometric and photometric data for this work.

Parameter	Parameter regime	Calibration choice	Reference
$\varpi^{\rm cal}$		Use `zpt.py` calibration	Lindegren et al. (2021b)
$\sigma_{\varpi}^{\rm cal}$		`uwu`$(G)\cdot$`parallax_error`	Fit to Fabricius et al. (2021) Fig. 19a&b
G	`astrometric_params_solved` = 95	Colour-dependent correction	Gaia Collaboration (2021e) Appendix A
$g_{\rm PS1}$	`g_mean_psf_mag` > 14	`g_mean_psf_mag` – 0.020	
$r_{\rm PS1}$	`r_mean_psf_mag` > 15	`r_mean_psf_mag` – 0.033	
$i_{\rm PS1}$	`i_mean_psf_mag` > 15	`i_mean_psf_mag` – 0.024	Scolnic et al. (2015)
$z_{\rm PS1}$	`z_mean_psf_mag` > 14	`z_mean_psf_mag` – 0.028	
$y_{\rm PS1}$	`y_mean_psf_mag` > 13	`y_mean_psf_mag` – 0.011	
$g_{\rm SM}, r_{\rm SM}$		$E(B-V)$ dependent zero-point shifts	Huang et al. (2021a)
$u_{\rm SM}, v_{\rm SM}$		Not used in inference	Schlafly et al. (2016)
$\sigma_{\rm mag}$	*Gaia* EDR3	$\max\{\sigma_{\rm mag,source}, 0.02{\rm mag}\}$	
	2MASS, AllWISE	$\max\{\sigma_{\rm mag,source}, 0.03\ {\rm mag}\}$	
	Pan-STARRS1 DR1	$\max\{\sigma_{\rm mag,source}, 0.04\ {\rm mag}\}$	
	SkyMapper DR2	$\max\{\sigma_{\rm mag,source}, 0.05\ {\rm mag}\}$	

3. Method: The StarHorse code

StarHorse (Queiroz et al. 2018) is an isochrone-fitting code tailored to derive distances d, extinctions (at $\lambda = 542$ nm) A_V, ages τ, masses m_*, effective temperatures $T_{\rm eff}$, metallicities [M/H], and surface gravities $\log g$ for field stars. In the absence of spectroscopic input data, it takes as input only the measured parallax ϖ and a set of observed magnitudes m_λ to estimate how close a stellar model is to the observed data.

StarHorse also includes priors about the geometry, metallicity and age characteristics of the main Galactic components. The priors adopted here are very similar to those in Queiroz et al. (2018), A19, and Queiroz et al. (2020): a Chabrier (2003) initial mass function; exponential spatial density profiles for thin and thick discs; a spherical halo and a triaxial bulge/bar component, as well as broad Gaussian distributions for the age and metallicity distribution priors. The normalisation of each Galactic component, as well as the solar position, were taken from Bland-Hawthorn & Gerhard (2016).

3.1. Code updates and improvements

With respect to A19 and Queiroz et al. (2020), we have implemented some changes that help to improve the performance of StarHorse in the context of *Gaia* EDR3.

3.1.1. A more informative interstellar extinction prior

One of the drawbacks of the A19 *Gaia* DR2 run was the a priori limit in interstellar extinction to $A_V < 4$ mag for sources with low signal-to-noise parallax measurements (`parallax_over_error` < 5). This resulted in poor convergence or biased results for distant obscured objects in the Galactic plane. For the present EDR3 run we therefore update our previously uninformative top-hat A_V prior to a prior that takes into account our knowledge of Galactic interstellar extinction.

For the region of the sky covered by Pan-STARRS1, we use the large-scale three-dimensional extinction map of Green et al. (2019). For the missing part (1/4) of the sky, we use the 2MASS-derived three-dimensional extinction model by Drimmel et al. (2003). To get the range of possible distances for each star (needed to query the extinction maps), we invert the EDR3 zero-point-corrected parallax measurements to estimate a prior extinction value range for each star (using a maximum of $A_{V_{\rm prior}} = 10$ mag, considering that our sample is limited by $G < 18.5$). The extinction prior is then defined as a very broad Gaussian distribution around the central value (with $\sigma_{AV,{\rm prior}} = \max\{0.2, 0.33 \cdot A_{V_{\rm prior}}\}$).

3.1.2. Extragalactic priors

In A19 we saw that the stellar populations of the Magellanic Clouds, the Sagittarius (Sgr dSph) galaxy, and a number of relatively nearby globular clusters, whose stellar densities were not accounted for by our priors until now, left a spurious imprint on the posterior Galactic density distribution inferred with StarHorse.

For the new runs we therefore included new extragalactic and globular cluster priors in the calculation of the global prior. For the extragalactic resolved stellar population we use the updated list (October 2019) of Local Group Galaxies from McConnachie (2012), which comprises sky positions, distances, foreground extinctions, apparent dimensions, central densities, metallicities, masses, and other basic quantities for the Local Group. We manually added M31 to this list, and curated the list for the most prominent objects on the sky: the Magellanic Clouds and the Sgr dSph galaxy. For all but these objects we estimate the mass of the external galaxy by inverting the mass-metallicity relation of Panter et al. (2008) (linearly extrapolated below [Fe/H] = −1). For the Galactic globular clusters we used the recent catalogue of Hilker et al. (2020).

The sky distribution of all considered objects is shown in Fig. 1. If a star's celestial coordinates coincide with those of an external galaxy or globular cluster within five half-light radii, we add to the Milky Way foreground prior an additional population corresponding to the characteristics of that object (stellar density, distance, metallicity). For the sake of simplicity, the density profile priors for all objects are assumed to be three-dimensional Gaussians.

3.1.3. Update of the bar angle in the priors

Our knowledge about the large-scale parameters of the Milky Way is constantly improving. In light of the growing evidence for a bar angle around 27 ± 2 deg (see discussion in Bland-Hawthorn & Gerhard 2016, reinforced also by Queiroz et al. 2021), we have updated the angle of the Galactic bar in our prior to that value.

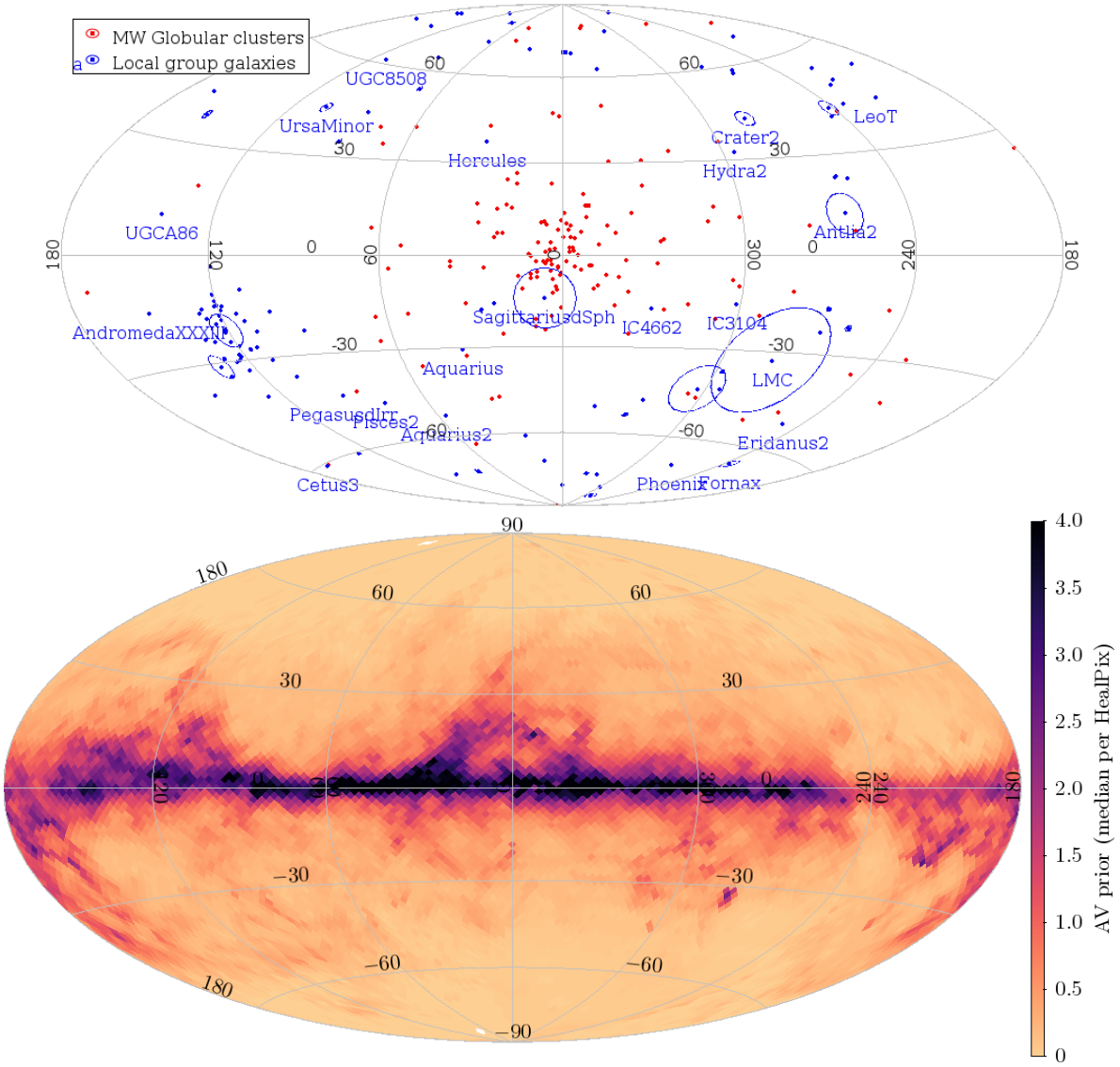

Fig. 1. Newly implemented priors in the `StarHorse` code. *Top panel*: sky distribution (in Galactic coordinates) of extragalactic and globular-cluster priors added in the new `StarHorse` version. The angular extents (5 effective radii) of each of the Local Group priors are shown as circles, highlighting the most prominent objects: the Magellanic Clouds, the Sgr dSph, and Andromeda. *Bottom panel*: median prior V-band extinction per HealPix. The extinction prior is calculated individually for each star from the three-dimensional extinction maps of either Green et al. (2019) or Drimmel et al. (2003).

3.1.4. Taking into account evolution of surface metallicity

We adopt here the latest version of the PARSEC1.2S + COLIBRI S37 stellar evolutionary model tracks (Bressan et al. 2012; Marigo et al. 2017; Pastorelli et al. 2019). Using these tracks in conjunction with the new CMD web interface allows us to take into account changes in the surface metallicity of stars during stellar evolution. While the effect is typically very small, element diffusion does introduce some small but appreciable decrease in the surface metal content for solar-mass stars before and around the turn-off (Fig. 2; see e.g. Bertelli Motta et al. 2018; Souto et al. 2019 for observational evidence). The effect is much stronger for low-metallicity stars. The opposite (i.e. a strong increase in the surface metallicity) happens for a fraction of the more evolved stars, such as those in the thermally pulsing asymptotic giant branch and Wolf-Rayet phases; this latter effect, however, is much less relevant to our results given that these evolutionary phases are much shorter-lived (and hence rarer) than main sequence stars, especially in nearby volume-limited samples.

3.2. `StarHorse` *setup*

For the EDR3 run we used a grid of PARSEC 1.2S stellar models (Marigo et al. 2017) in the 2MASS, Pan-STARRS1, SkyMapper, *Gaia* EDR3, and WISE photometric systems available on the PARSEC web page[3]. The model grid was equally spaced by 0.1 dex in log age as well as in initial metallicity [M/H]. The code explores distances within $\{1/(\varpi^{\rm cal} + 3\cdot\sigma_{\varpi}^{\rm cal}), 1/(\varpi^{\rm cal} - 3\cdot\sigma_{\varpi}^{\rm cal})\}$.

For the present *Gaia* EDR3 run ($G < 18.5$ mag, 400M stars), the code took on average 0.3 s per star to run (depending slightly on the position in the CMD and the number of photometric measurements available). In total, the computational cost for this

[3] `http://stev.oapd.inaf.it/cgi-bin/cmd_3.4`; see also `http://stev.oapd.inaf.it/cmd_3.4/faq.html`

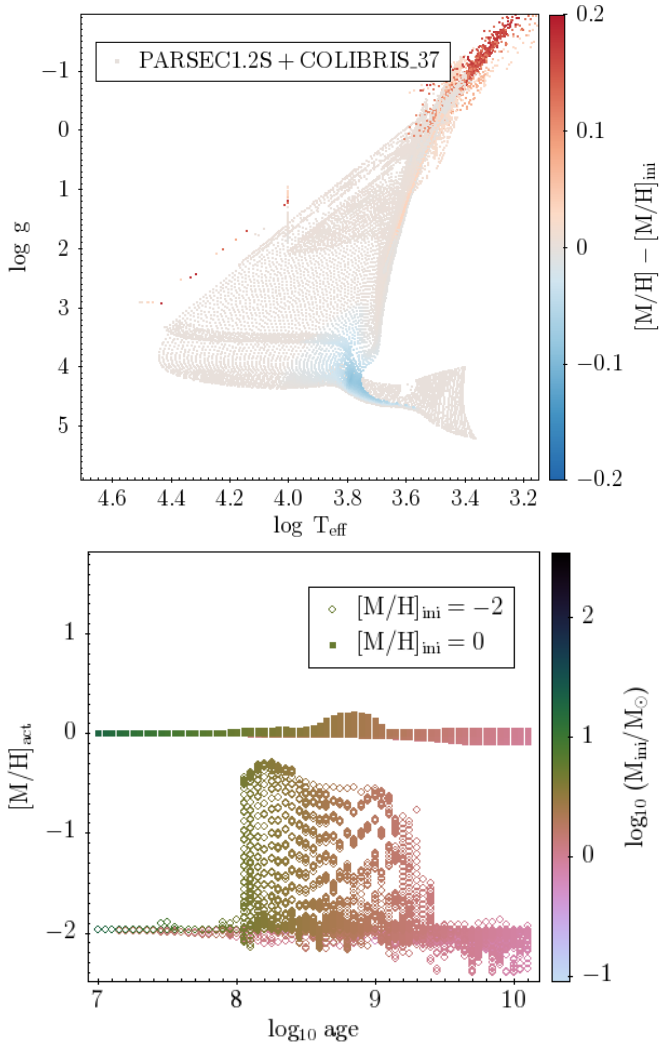

Fig. 2. Stellar evolution effects on surface metallicity in the PARSEC 1.2S + COLIBRI S37 stellar models. *Top*: Kiel diagram colour-coded by the difference between the surface metallicity and the initial metallicity. The evolution effects of diffusion and dredge-up are clearly visible. *Bottom*: age dependence of the surface metallicity, for two initial metallicities, colour-coded by stellar mass.

StarHorse run thus was ~50 000 CPU hours, reducing the CO_2 footprint of StarHorse by a factor of 3 with respect to the *Gaia* DR2 run presented in A19, while increasing the number of stars with reliable output parameters by more than a factor of 2. The global statistics for our output results are summarised in Table 2 and discussed in detail in Sect. 4.

3.3. Input and output flags

Along with the output of our code (median statistics of the marginal posterior in distance, extinction, and stellar parameters), we provide a set of flags to help the user decide which subset of the data to use for their particular science case. These flags correspond to the columns defined in the next few subsections.

3.3.1. *Gaia* EDR3 quality criteria used in this work

In the previous StarHorse *Gaia* DR2 run, we defined a set of input flags (summarised in the column SH_GAIAFLAG) based on the DR2 recommendations by the Gaia Collaboration (e.g. Lindegren et al. 2018). It contained three digits corresponding to astrometric fidelity (in particular the renormalised unit-weight error, ruwe; Lindegren 2018), the photometric fidelity (indicated by the phot_bp_rp_colour_excess), as well as the DR2-native variability_flag.

In this work we make use of the quality criteria established by Rybizki et al. (2022) and Riello et al. (2021) who have addressed these questions in detail and provide recipes to select high-quality EDR3 measurements. We thus follow their recommendations and use the following cuts:

Astrometric fidelity: We cross-matched our catalogue with the astrometric fidelity flag defined by Rybizki et al. (2022), based on a neural-network classifier for EDR3 objects. The classifier uses the twelve EDR3 astrometric columns identified by Gaia Collaboration (2021b) as containing most information about the fidelity of the EDR3 parallaxes and proper motions (and their uncertainties). It was trained on a set of bona fide trustworthy and bona fide bad EDR3 results. Bad astrometric results can be culled by requiring, for example, fidelity > 0.5.

Colour excess factor: The corrected version of the EDR3 phot_bp_rp_colour_excess column, C_* or bp_rp_excess_corr (Riello et al. 2021, see also Appendix B of Gaia Collaboration 2021e), indicates whether the BP/RP photometry of a *Gaia* source may be affected by background flux from neighbouring objects. When cleaning the StarHorse results for potentially affected BP/RP photometry, we recommend using a cut of $|C_*|/\sigma_{C^*} < 5$, where σ_{C^*} is a simple function of the G magnitude, computed according to Eq. (18) in Riello et al. (2021).

3.3.2. sh_photoflag

As in A19, we define the human-readable sh_photoflag that contains the information about the combination of photometric input data used for each object (*Gaia* EDR3, PS1, SkyMapper, 2MASS, AllWISE). For example, if only *Gaia* EDR3 G, G_{RP} and 2MASS HK_s magnitudes were available, the flag reads GRPHKs. PS1 and SkyMapper photometry are separated by a slash (/) in the sh_photoflag: for example, the flag Gg/riW1W2 means that the object in question has good *Gaia* G, PS1 g, SkyMapper ri, and AllWISE $W1W2$ measurements, while G/g means that the object has only *Gaia* G and SkyMapper g.

We note that with respect to A19 we improved the quality filters especially for the input AllWISE and 2MASS data, as well as for the *Gaia* BP/RP photometry (see Sect. 2).

3.3.3. sh_outflag

In A19, we defined a StarHorse output flag, consisting of five digits that informed about the fidelity of the StarHorse output parameters. The first digit served as the main quality indicator and filtered out stars with inconsistent median output parameters. Although the main caveats of the A19 results have been rendered obsolete by EDR3, we still define an output flag for convenience. It contains the following four digits:

The first digit flags low number of consistent models. For some targets, the number of stellar models in our model grid found to be 3σ-consistent with the data is low, indicating either very precise results or (more likely) some tension in the input data. We consider a results unproblematic if the number of models is greater than 30, and apply a (strong) warning flag if this number is between 10 and 30 (below 10): IF nummodels > 30 THEN 0 ELIF nummodels > 10 THEN 1 ELSE 2.

Table 2. Global statistics of some of the currently available astrometric and astro-photometric results based on *Gaia* DR2 and EDR3 data, in comparison to this work.

Reference	Data used	Mag limit	# objects	$\sigma_d/d^{G=17}$	$\sigma_{A_V}^{G=17}$	$\sigma_{T_{\rm eff}}^{G=17}$
Bailer-Jones et al. (2018b)	DR2 parallaxes	$G \lesssim 21$	1330M	24%	–	–
Andrae et al. (2018)	DR2 photo-astrometry	$G \leq 17$	161M	–	–	324 K
			88M	–	0.46 mag	–
Anders et al. (2019)	DR2 + 2MASS+AllWISE	$G < 18$	266M	40 %	0.25 mag	350 K
flag-cleaned sample	+Pan-STARRS1		137M	18 %	0.23 mag	230 K
Green et al. (2019)	DR2 + 2MASS+Pan-STARRS1	$z_{PS1} < 20.9$	799M	20 %	0.15 mag	–
Bai et al. (2019, 2020)	DR2 photo-astrometry	$G \lesssim 17$	133M	–	0.16 mag	350 K
Bailer-Jones et al. (2021)	EDR3 parallaxes	$G \lesssim 21$	1470M	20 %	–	–
	EDR3 photo-astrometry		1310M	16 %	–	–
This work	EDR3 photo-astrometry	$G < 18.5$	402,431,354			
`StarHorse` converged	+2MASS		362,392,321	15 %	0.15 mag	183 K
& `fidelity` > 0.5	+AllWISE		329,646,544			
& $\lvert C^* \rvert / \sigma_{C^*} < 5$	+Pan-STARRS1		321,131,855			
& `sh_outflag`==“0000”	+SkyMapper		281,501,963			

Notes. $^{G=17}$For comparability, we report here the median precision for stars at magnitude $G \approx 17$.

The second digit flags negative extinction. Significantly negative extinctions should be treated with care: IF `AV95` > 0 THEN 0 ELSE 1.

The third digit warns about very large uncertainties. Large uncertainties are not problematic per se, but the corresponding median values are not usually very informative, which is why we provide this flag to be able to filter out very uncertain results quickly. The definition is as follows: IF $0.5 * (\texttt{dist84} - \texttt{dist16})/\texttt{dist50} > 1$ OR $0.5 * (\texttt{AV84} - \texttt{AV16}) > 1$ OR $0.5 * (\texttt{teff84} - \texttt{teff16}) > 1000$ OR $0.5 * (\texttt{logg84} - \texttt{logg16}) > 1$ OR $0.5 * (\texttt{met84} - \texttt{met16}) > 1$ OR $0.5 * (\texttt{mass84} - \texttt{mass16})/\texttt{mass50} > 1$ THEN 1 ELSE 0.

The fourth digit flags very small uncertainties. Very small posterior uncertainties are most likely underestimated and probably indicate poor convergence. These results should also be used with care. The definition is as follows: IF $0.5 * (\texttt{dist84} - \texttt{dist16})/\texttt{dist50} < 0.001$ OR $0.5 * (\texttt{av84} - \texttt{av16}) < 0.01$ OR $0.5 * (\texttt{teff84} - \texttt{teff16}) < 20.$ OR $0.5 * (\texttt{logg84} - \texttt{logg16}) < 0.01$ OR $0.5 * (\texttt{met84} - \texttt{met16}) < 0.01$ OR $0.5 * (\texttt{mass84} - \texttt{mass16})/\texttt{mass50} < 0.01$ THEN 1 ELSE 0.

Unproblematic results from the point of view of `StarHorse` can thus be filtered by requiring `sh_outflag`==“0000”.

4. `StarHorse` *Gaia* EDR3 results

4.1. Summary

Table 2 summarises the results of the `StarHorse` run for *Gaia* EDR3 as well as previous results available from the recent literature. We observe that our new `StarHorse` results compare favourably in terms of both sample size and parameter precision. For example, the results have notably improved in precision (typically shrinking the formal uncertainties by a factor of 2) with respect to A19 (see Sect. 6 for a more detailed comparison).

Figure 3 shows the distribution of the `StarHorse` median posterior output values $T_{\rm eff}$, $\log g$, [M/H], M_*, d, and A_V and their corresponding uncertainties, demonstrating the complexity of the dataset as well as the typical precision (discussed in more detail in Sect. 5.1). Even the median output parameters are highly correlated, either intrinsically (enforced by the stellar models, e.g. $T_{\rm eff}$ vs. $\log g$), due to selection effects (e.g. d vs. M_*), or because of degeneracies related to our method ($\sigma_{T_{\rm eff}}$ vs. σ_{A_V}). The gridding effect in the metallicity panels of Fig. 3 is due to the finite resolution of the model grid.

Figure 4 shows the sky distribution of the input sample (400 M stars with $G < 18.5$), as well as sky maps of the percentage of converged sample and the cleaned sample. The figure shows that the code convergence is lowest in the densest areas of the sky (the innermost bulge and Galactic plane as well as the centre of the Large Magellanic Cloud), and that cleaning the *Gaia* data enhances this effect. For example, the X shape in the inner bulge visible in the bottom panel of Fig. 4 is mainly produced by the quality cut in the *Gaia* EDR3 colour excess factor (compare to Fig. 21 of Riello et al. 2021).

In the following subsections, we present some immediate results that can be obtained from our catalogue, focussing on CMDs (Sect. 4.2), Kiel diagrams (Sect. 4.3), stellar density maps (Sect. 4.4), and extinction maps (Sect. 4.5).

4.2. Extinction-corrected colour-magnitude diagrams

Since the stellar models used in our Bayesian inference have not changed much with respect to A19, the `StarHorse` extinction-corrected CMDs are also similar. The top row of Fig. 5 shows the CMD of the total sample and two interesting subsamples (the *Gaia*-cleaned sample and the fully flag-cleaned sample). When comparing these panels to Fig. 5 in A19, we note that some of the previously noted unphysical features have disappeared (most notably, the ‘nose’ between the main sequence and the lower red-giant branch). On the other hand, new structure in the top parts of the full CMDs emerges from the explicit inclusion of the Magellanic Clouds in the priors. For illustration, the bottom row of Fig. 5 shows the populations of the Milky Way disc, the Large Magellanic Cloud (LMC), and the Small Magellanic Cloud (SMC).

The second row of Fig. 5 shows the CMDs for three bins in apparent magnitude. The overall appearance of the magnitude-binned CMDs in Fig. 5 resembles those of Fig. 4 in A19, with a few notable differences. For example, in addition to the sharp features of single-star evolution in the $G < 14$ panel, we now also appreciate the unresolved binary sequence right above the low-mass main sequence. We also see the impact of the LMC and SMC populations on the CMD, already in the magnitude bin $16 < G < 17$. The rightmost middle panel, corresponding to $18 < G < 18.5$, shows already significant broadening in the

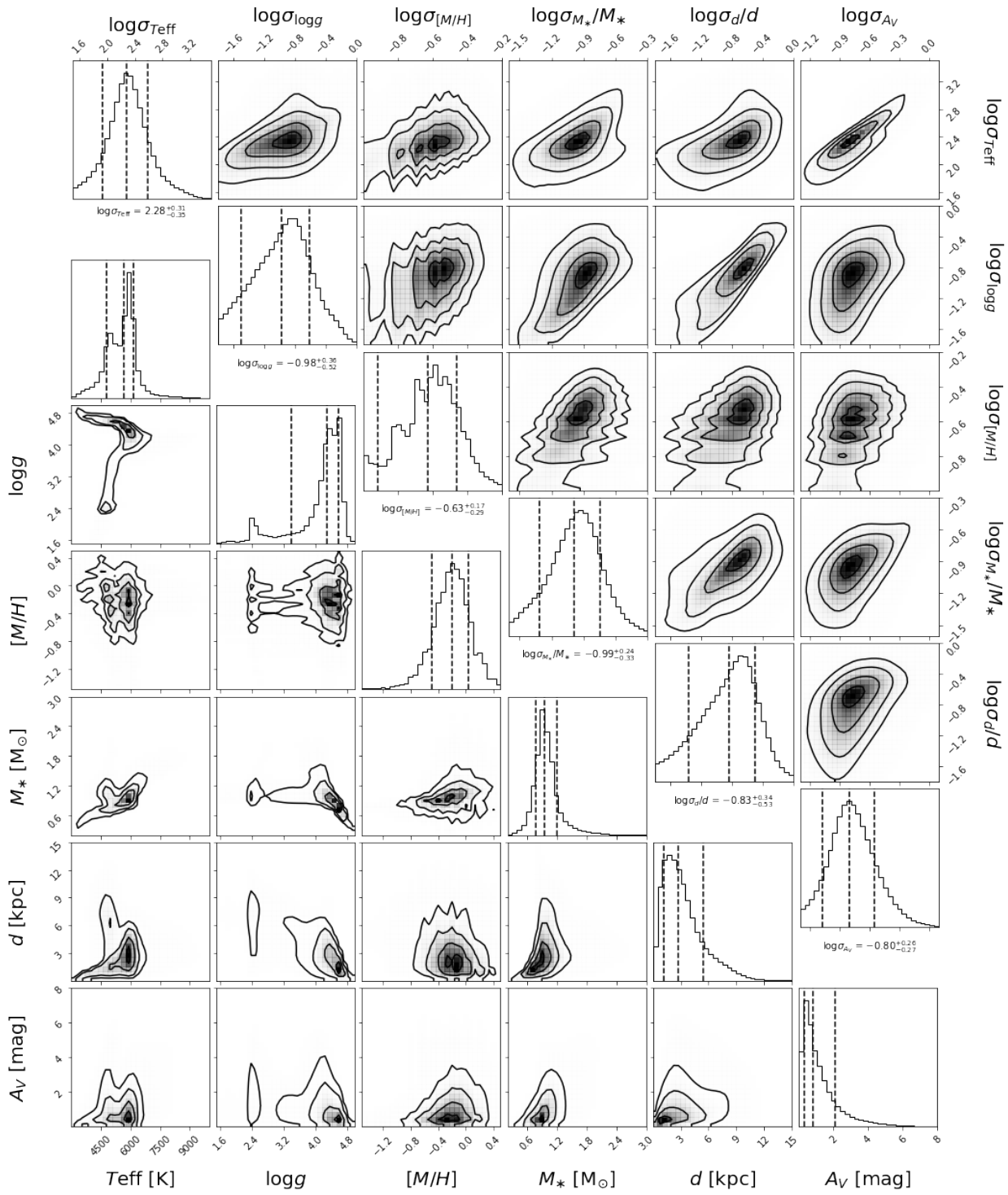

Fig. 3. `corner` plots showing the correlations and distributions of `StarHorse` median posterior output values $T_{\rm eff}$, $\log g$, [M/H], M_*, d, and A_V (*lower-left panels*), and their corresponding uncertainties (in logarithmic scale; *top-right panels*) for all stars in our catalogue. The dashed vertical lines in the diagonal panels show the 16th, 50th, and 84th percentiles of each parameter.

CMD features. As in A19, this is a result of the growing uncertainty in the input parameters, especially the parallax. We also recall that the absolute magnitudes and de-reddened colours displayed in Fig. 5 are not a direct output of `StarHorse`, but were computed from the observed magnitudes and the `StarHorse` median distance, extinction, and effective temperatures[4].

[4] https://github.com/fjaellet/gaia_edr3_photutils

4.3. Kiel diagrams

Figure 6 shows Kiel diagrams ($T_{\rm eff}$ vs. $\log g$) for the full *Gaia* EDR3 `StarHorse` sample. The density plot (left panel) shows that most of the sample is classified as FGK stars, as expected. Also clearly visible (both in the left and the middle panel) are the stripe-like overdensities corresponding to the metallicity resolution of the stellar model grid already noted in Sect. 4.1.

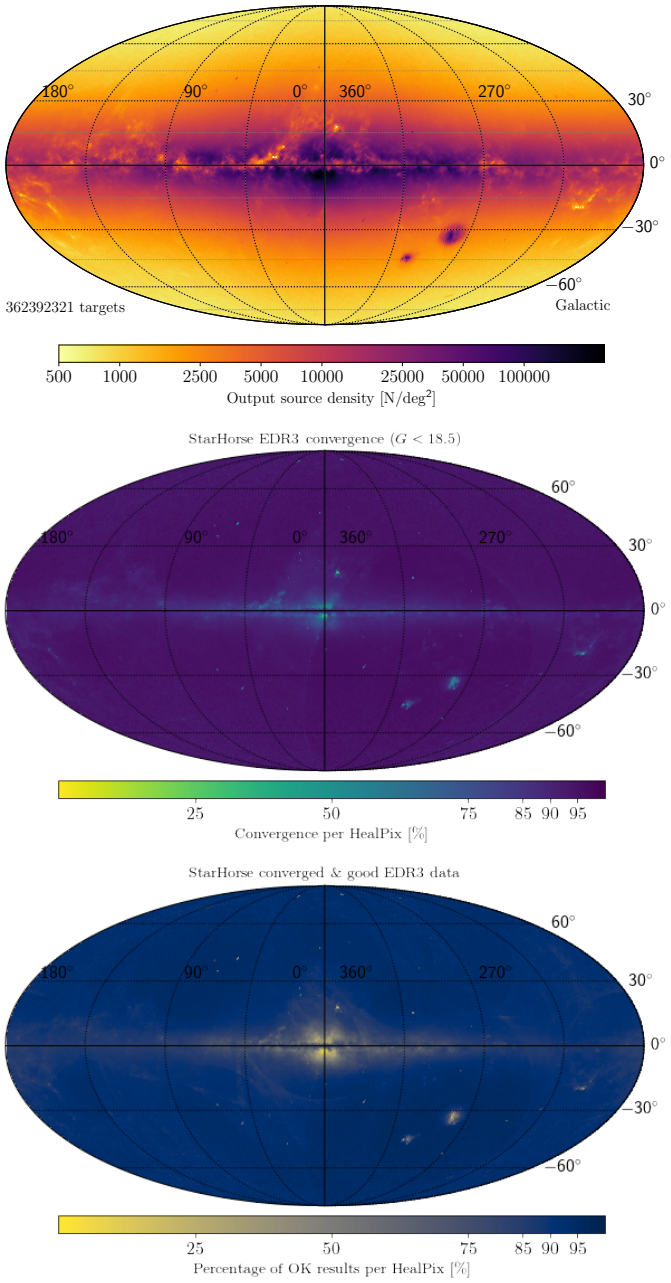

Fig. 4. Sky density map of all converged targets ($G < 18.5$ mag; *top panel*). *Middle and bottom panels*: relative fraction of converged stars and flag-cleaned results with respect to the input data.

We note a much more defined horizontal branch with respect to A19, which is at least in part due to the metallicity prior for globular clusters. We also note a more populated pre-main sequence (region above the lower main sequence), since we now applied a slightly less restrictive age cut ($\log t > 7$, as compared to $\log t > 7.5$ in A19).

The middle panel of Fig. 6 (Kiel diagram colour-coded by metallicity) shows that the posterior metallicity information is consistent with the stellar model grid through most of the parameter space. The only few outliers from the space spanned by the stellar models are stars whose median output parameters lie in-between the main sequence and the giant branch (due to a significantly bimodal posterior). The number of those stars (for which the median `StarHorse` are unreliable) has diminished enormously with respect to A19.

Finally, the right panel of Fig. 6 shows the typical distance range sampled for different regions of the Kiel diagram (also visible in Fig. 3), showing the expected behaviour of large typical distances (even >100 kpc) for the most luminous stars and very small distances for the coolest and least massive dwarf stars (<100 pc; see e.g. Gaia Collaboration 2021b).

4.4. Stellar density maps

4.4.1. Overall density distribution

One of the main motivations for the `StarHorse` project is Galactic cartography, and some of the newly implemented changes in the code (see Sect. 3.1) result in a visible improvement of the stellar density maps. To illustrate this, Fig. 7 shows two-dimensional projections of the stellar density distribution for the full `StarHorse` sample in Cartesian galactocentric coordinates. The left column of the plot focuses on larger structures: the Galactic volume probed by *Gaia* and the neighbouring dwarf galaxies, as indicated in each panel. These populations are now clearly visible as overdensities in the maps, although a considerable amount of stars still has median distances that fall in between the Magellanic Clouds and the Milky Way – a result of the multimodal posterior distance distributions (see e.g. Anders et al. 2019).

The right panels of Fig. 7 zoom into a 20 kpc wide cube centred on the Sun. When we compare these maps to the ones presented in Fig. 7 of A19, we notice: 1. the increase in total stellar number density (from 137 million to 360 million stars), and 2. the greater volume probed by the *Gaia* EDR3 $G < 18.5$ sample.

Direct consequences of the maps shown in Fig. 7 for Galactic cartography, however, are not obvious, since these maps are the result of a complex convolution of the true stellar density distribution, interstellar extinction, the applied magnitude limit, the selection function, and the priors. In the following subsections, we discuss the density maps of some specific stellar populations that are arguably easier to interpret.

4.4.2. Red-clump stars

Core helium burning red-clump stars (for a review see Girardi 2016) are often used as standard candles for mapping Galactic populations. They are numerous, relatively bright, and span a wide range of ages and metallicities.

Figure 8 shows the distribution of disc red-clump stars in the `StarHorse` *Gaia* EDR3 catalogue. The stars have been selected using the Kiel diagram as in Sect. 4.4 of A19: 4500 K < $T_{\rm eff}$ < 5000 K, 2.35 < $\log g$ < 2.55, −0.6 <[M/H]< +0.4, $|Z| < 3$ kpc. Figure 8 can thus be directly compared to Fig. 8 in A19.

In Fig. 8 of A19 we observed a very clear overdensity of red-clump stars tracing the Galactic bar. This result was all the more convincing since the bar angle used in the prior was significantly different from the one observed in the posterior distribution. However, Fig. 8 of A19 also displayed some minor artefacts, such as underdensities of red-clump stars both in front of and behind the near side of the bar, or an underdense ring-like structure that arose from the quality cuts necessary to clean the DR2 `StarHorse` data.

The EDR3 version of that figure, shown in Fig. 8, shows that the result of A19 (the detection of the Galactic bar in stellar density) is clearly maintained. The number of red-clump stars has become greater (13.8M vs. 10.8M), the underdensity artefacts of

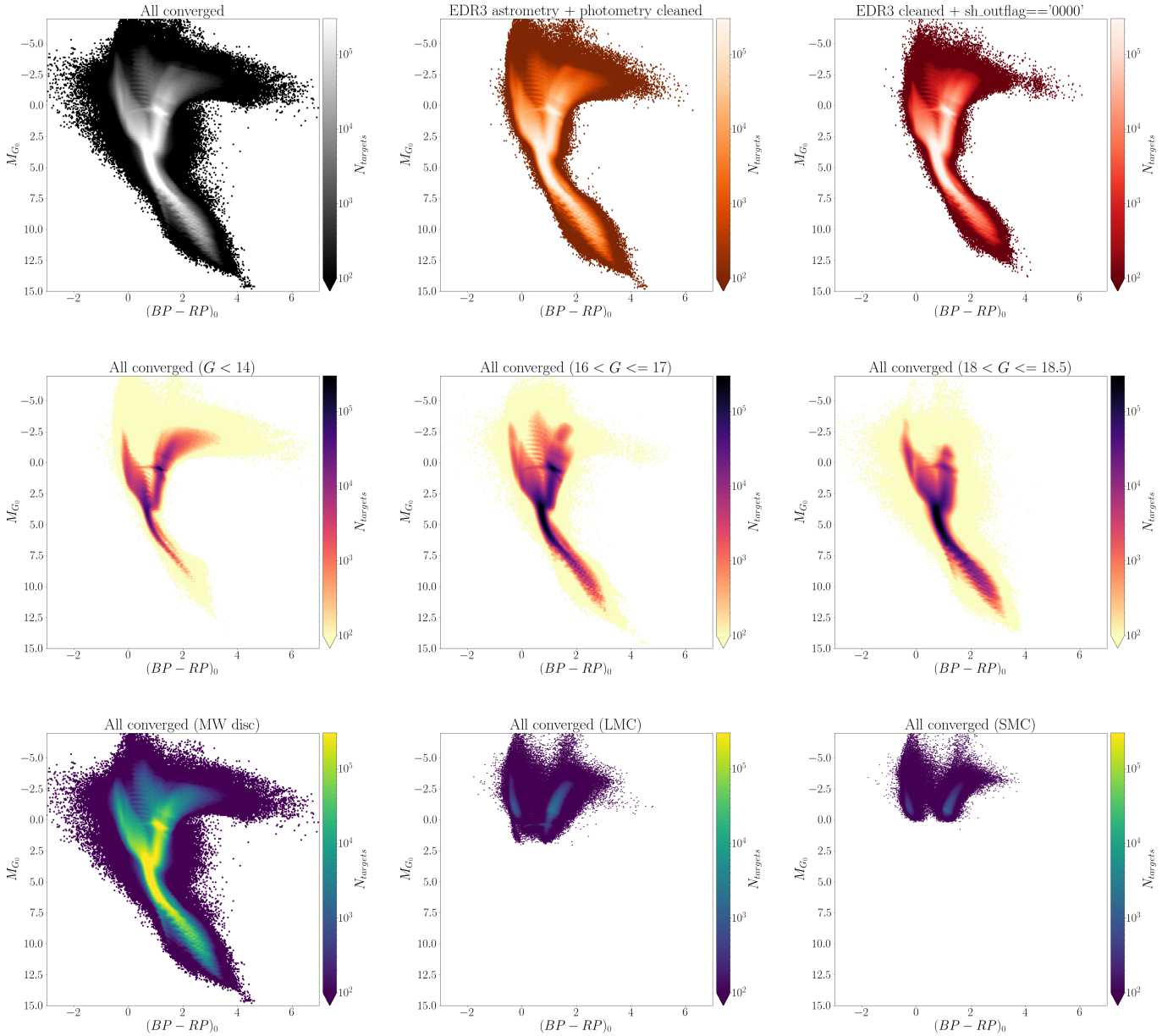

Fig. 5. StarHorse posterior *Gaia* EDR3 CMDs. *Top row, from left to right*: all converged objects (362M), *Gaia* EDR3 cleaned sample (321M), EDR3- and flag-cleaned sample (282M). *Middle row*: CMDs for three broad magnitude bins, showing both the increasing mix of stellar populations (e.g. the giant-star populations of the Magellanic Cloud starting to appear around $M_G \sim -3$ in the $16 < G < 17$ panel) and the decreasing astrometric quality with increasing magnitude. *Bottom row*: separate CMDs for the Milky Way disc (*left*; 339M stars), the LMC (*middle*; 1.09M stars), and the SMC (*right*; 94k stars). The abrupt absolute magnitude cut in the last two panels is caused by the $G < 18.5$ mag cut.

the map are greatly reduced, and the probed Galactic area now extends to regions beyond the (near side of the) bar.

The apparent bar angle is similar to the one in Fig. 8 of A19 and thus still appears to be a few degrees higher than the one assumed in the prior (27 deg; see Sect. 3.1.3). The main overdensity of the bar also appears relatively short compared to recent estimates of $\gtrsim$5 kpc. A quantitative analysis of the bar's structural parameters is, however, beyond the scope of this paper, as this requires careful modelling (e.g. Wegg et al. 2015; Portail et al. 2017) and taking into account selection effects.

Another feature in Fig. 8 is an overdensity appearing around $R_{\rm Gal} \sim 6$ kpc that might correspond to the Sagittarius spiral arm (see e.g. Reid et al. 2019). This feature is much less clear in the red-clump stars than in maps of young stellar populations (e.g. Castro-Ginard et al. 2021; Zari et al. 2021; Poggio et al. 2021), and the map in Fig. 8 shows the underlying density distribution convolved with dust extinction and other selection effects. The clear overdensity in the (logarithmic) red-clump star count map is, however, a strong feature that deserves further investigation, since the strength of the spiral density signature in an intermediate-age population has implications on the modelling of the Milky Way's spiral arms.

Recently, Nogueras-Lara et al. (2021) have used the high angular-resolution infrared photometric survey GALACTICNUCLEUS (Nogueras-Lara et al. 2019) to determine the distances, extinctions, and stellar populations of the inner spiral arms in a small region of the sky containing the Galactic centre. While their data are of clearly superior quality, we suggest that

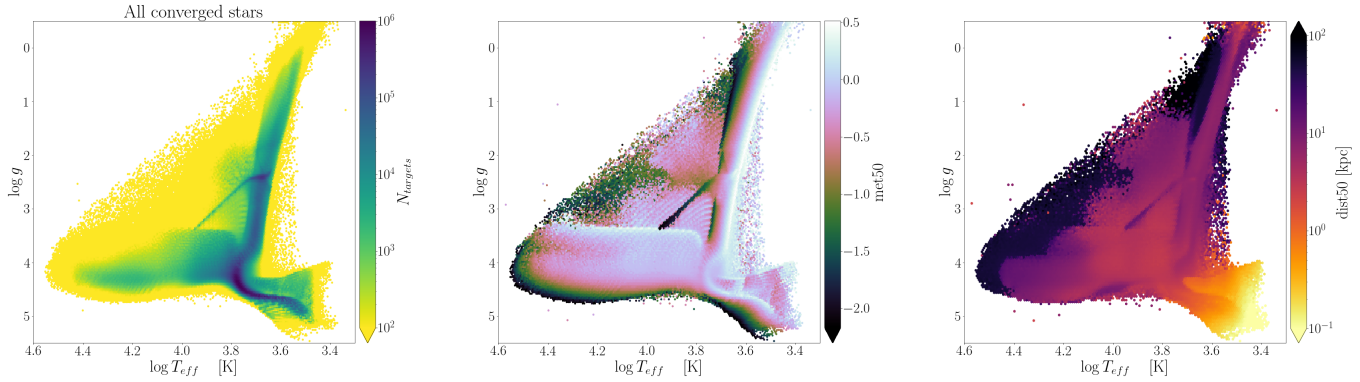

Fig. 6. `StarHorse`-derived Kiel diagrams (before applying any quality cuts). *Left*: density plot. *Middle*: colour-coded by median metallicity. *Right*: colour-coded by median distance.

similar mapping studies could be carried out using *Gaia* and multi-wavelength photometry (and possibly our `StarHorse` catalogue) for the portions of the disc less affected by interstellar extinction.

4.4.3. Magellanic Clouds

The Magellanic Clouds as our immediate galactic neighbours represent a key laboratory to study gravitational interactions and their effects on the structure and kinematics of satellite galaxies. In this section, we analyse our results for the region of the Magellanic Clouds and compare them to the Gaia Collaboration (2021d) results.

In Fig. 9 we show from top to bottom the sky density map, 2D distance distribution, metallicity and extinction maps for the sources around the Large Magellanic Cloud (LMC, left) and Small Magellanic Cloud (SMC, right), respectively, in equatorial coordinates.

For the LMC (left column of Fig. 9), the sky density distribution highlights the main components of the galaxy. The innermost contour encloses the elongated bar, while the second contour highlights the spiral arm. We notice a small region with low star density between the bar and the spiral arm, in agreement with the star counts shown in Gaia Collaboration (2021d, e.g.), but much less smooth, because of the relatively low convergence rate of `StarHorse` in that region (due to crowding issues in the input data; see Fig. 4).

The distance map (second row of Fig. 9) indicates a median heliocentric distance of 49.4 kpc (for comparison, the distance used in the prior is $d_{\rm prior}$ = 50.58 kpc; McConnachie 2012), for the sources inside the outermost contour level, in agreement with previous estimations (e.g. Pietrzyński et al. 2019). It also shows the expected distance gradient from the fact that the LMC is inclined about 34°, being the closer side the one towards larger declinations (Gaia Collaboration 2021d, and references therein).

The LMC metallicity map (third row left panel of Fig. 9) highlights a problematic result: In the inner parts of the LMC, we see a positive metallicity gradient from the bar region towards the outer disc, opposite to the trend observed with red-giant branch (RGB) stars from Magellanic Cloud Photometric Survey (MCPS) and OGLE-III (Choudhury et al. 2016), RR Lyrae stars from OGLE-IV (Skowron et al. 2016), or RGB stars from *Gaia* DR2 (Grady et al. 2021). The median metallicity in the bar region (inside the innermost contour level) is of −0.77 dex, while at the outer disc (between the innermost and outermost levels) is of −0.68 dex. This suggests that the little metallicity information contained the broad-band colours we use in this work is affected by significant systematics, at least for the very dense and complex regions of the Magellanic Clouds. The declining influence of the LMC prior biases the resulting median metallicities and inverts the expected trend (this can possibly be remedied when using the full posterior; see Appendix B).

Analogously, the right column of Fig. 9 shows the corresponding plots for the SMC sample. The sky distribution (top-right panel of Fig. 9) highlights the irregular structure of the SMC and the beginning of the bridge towards the direction of growing right ascension (and decreasing declination). The distance map (second row right panel of Fig. 9) provides a median distance to the SMC of 63.2 kpc (prior: $d_{\rm prior}$ = 63.97 kpc), for the sources inside the outermost level, in agreement with previous estimations (e.g. Cioni et al. 2000). The outer ring with closer distances may be partly an artefact due to the vanishing of the prior contribution towards the outer regions. No clear distance gradient is visible in the SMC.

Two small blobs with slightly smaller distance are visible in the central parts of the SMC, which are also correlated with the metallicity. Again, a small positive metallicity gradient from the inner towards the outer parts of the galaxy is visible, opposite to the expected behaviour observed with the Red Giant Branch sources from MCPS and OGLE-III (Choudhury et al. 2018) or *Gaia* DR2 (Grady et al. 2021). As in the LMCANDE0890215004, the metallicity and extinction appear to be correlated, being the extinction higher towards the central more crowded region of the galaxy (see bottom-right panel of Fig. 9).

4.4.4. Candidate metal-poor stars

The study of metal-poor stars provides a unique window into the formation and accretion history of our Galaxy, since the bulk of those stars were formed at high redshift and conserve abundance patterns unique to their site of formation (Beers & Christlieb 2005).

Although the broad-/intermediate-band photometry used in this work is only marginally sensitive to metallicity (in fact, only when including optical *griz* photometry can we expect to detect some metallicity information; see Sect. 5), low metallicities may manifest themselves in the broad-band colours (especially in the ultraviolet; e.g. Norris et al. 1999). We therefore venture to look at candidate metal-poor stars as determined by `StarHorse`, by defining a candidate metal-poor sample as `met84` < −1,

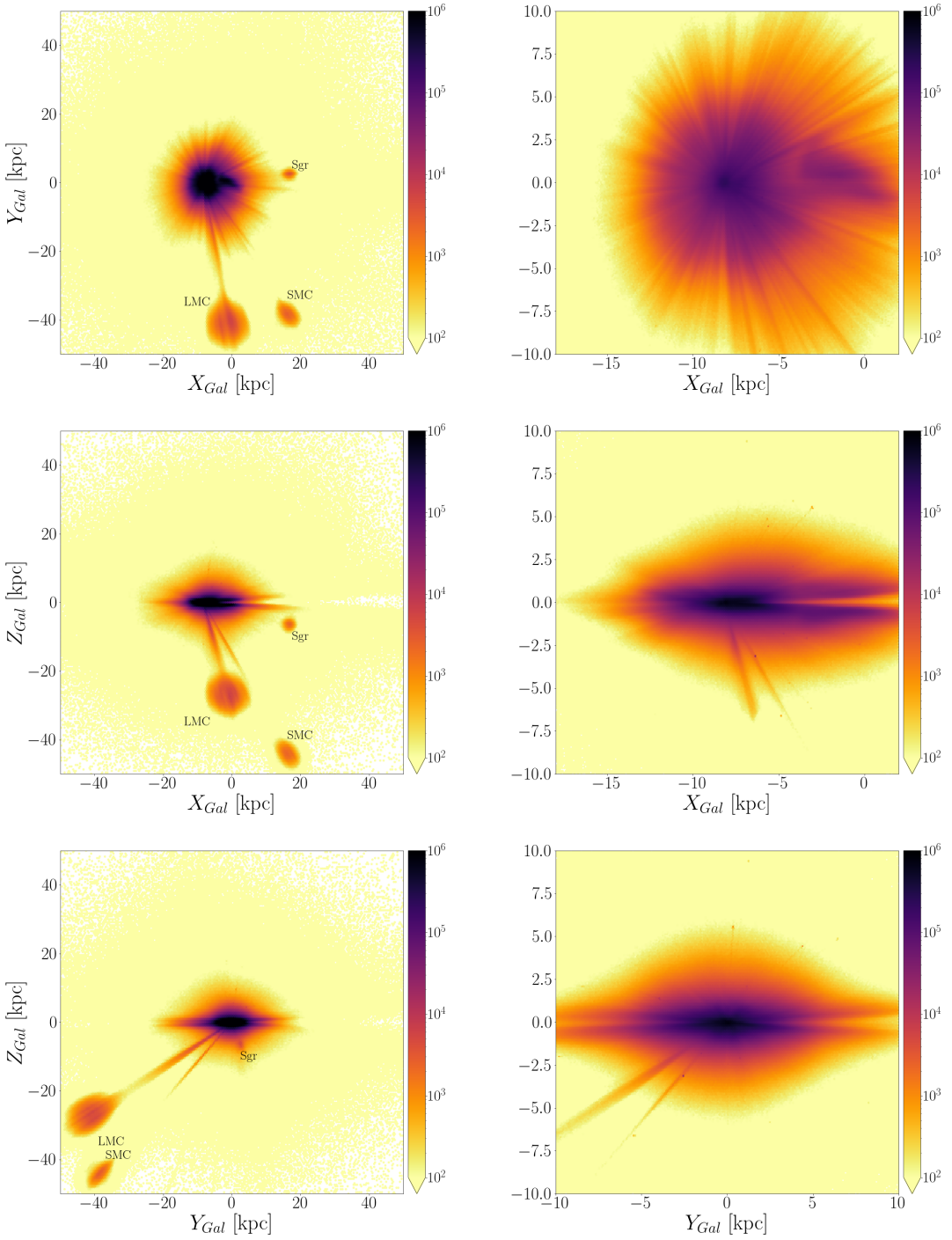

Fig. 7. StarHorse density maps (*from top to bottom*: *XY*, *XZ*, and *YZ*) in galactocentric coordinates. *Left column*: 100 kpc wide cube centred on the Galactic centre, while *right column*: zooms into a 20 kpc wide cube centred on the Sun.

corresponding to a 1σ confidence-level cut. This selection yields 1.58 million objects (without applying any further quality cuts).

Figure 10 shows the distribution of the metal-poor candidates in galactocentric cylindrical coordinates ($R_{\rm Gal}$ vs. $Z_{\rm Gal}$). We clearly see the imprint of the globular-cluster priors in this figure: All noticeable point-like overdensities correspond to prominent globular clusters, as annotated in the plot. We also note the overdensities in the direction of the Magellanic Clouds, corresponding to stars with bimodal distance probability density function (PDFs), resulting in a median distance in-between the inner halo and the Magellanic Clouds (see Sect. 4.4.3). A similar, less obvious structure, is also visible in the direction of the core of the Sgr dSph galaxy (located towards $(l, b) \sim (5, -14)$), resulting in an elongated overdensity around $(R_{\rm Gal}, Z_{\rm Gal}) \sim (0-3, -1)$.

Apart from these expected features, we also note a very prominent overdensity of local dwarf stars, many of them also following a disc-like density profile, and a diffuse overdensity in the nearby Galactic halo. The disc-like overdensity is likely mostly due to sample contamination, although even very metal-poor stars have been found on disc-like orbits recently in the Milky Way (Sestito et al. 2020) as well as in simulations (Sestito et al. 2021). The diffuse overdensity at larger

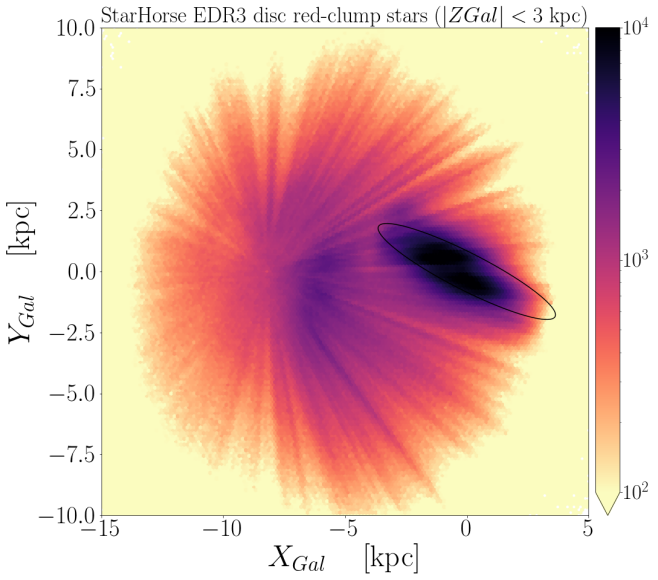

Fig. 8. XY density map, selecting all (13.8M) red-clump stars less than 3 kpc away from the Galactic midplane. The ellipse shows the orientation (27 deg with respect to the Sun-Galactic centre line) and approximate extent (semi-major axes $a = 4.07$ kpc and $b = 0.76$ kpc) of the Galactic bar assumed in the prior.

heliocentric distances is produced by more distant giant stars of the inner halo, expected from the combination of our selection function ($G < 18.5$) and our halo prior. Its members can be regarded as potential targets for future/ongoing spectroscopic surveys. Another possible overdensity is seen in the central parts of the Galaxy, where indeed many of the Milky Way's oldest stars are expected to reside (e.g. Tumlinson 2010; Koch et al. 2016; Starkenburg et al. 2017; Horta et al. 2021; Queiroz et al. 2021).

Although methods explicitly tailored to detect metal-poor star candidates from combined broad- and narrow-band colours can be expected to perform much better (e.g. Beers et al. 1985; Youakim et al. 2017; Da Costa et al. 2019; Thomas et al. 2019; Arentsen et al. 2020; Chiti et al. 2021; Huang et al. 2021b), our approach yields a large number of metal-poor star candidates for possible follow-up observations with multi-object spectroscopic surveys such as 4MOST (de Jong et al. 2019; Chiappini et al. 2019; Helmi et al. 2019).

4.4.5. Outer halo and Local Group

Figure 11 focuses on the density distribution of distant stars in the Galactic halo (defined by $|b| > 15$ deg, `dist50` > 10 kpc). The two top panels (showing Aitoff projections of the sky in ecliptic coordinates) highlight the long tidal tails of the Sgr dSph galaxy, also called the Sgr stream (e.g. Law et al. 2016). This feature, although not included in our priors, appears clearly both in the density map (top panel of Fig. 11) and the median distance map (middle panel), superseding the extent of the previous membership maps of the Sgr stream, for example the one produced by Antoja et al. (2020) based on *Gaia* DR2 proper motions.

The lower panel of Fig. 11 shows that the $G < 18.5$ sample encompasses also a significant amount of individual stars in dwarf galaxies of the Local Group other than the Magellanic Clouds and the Sgr dSph. For many of them (e.g. the Draco dSph, Bootes I, the Carina dSph, or the Ursa Minor dSph), the more informative extragalactic priors of the new `StarHorse` results can help to improve membership probabilities. For others (e.g. Sculptor dSph, Fornax dSph), the prominent pencil-beams between the halo and the expected location of the respective dwarf galaxy hint a problematic prior (e.g. imprecise central coordinates or too low galaxy masses in the Local Group tables used) that results in typically bimodal distance posterior PDFs.

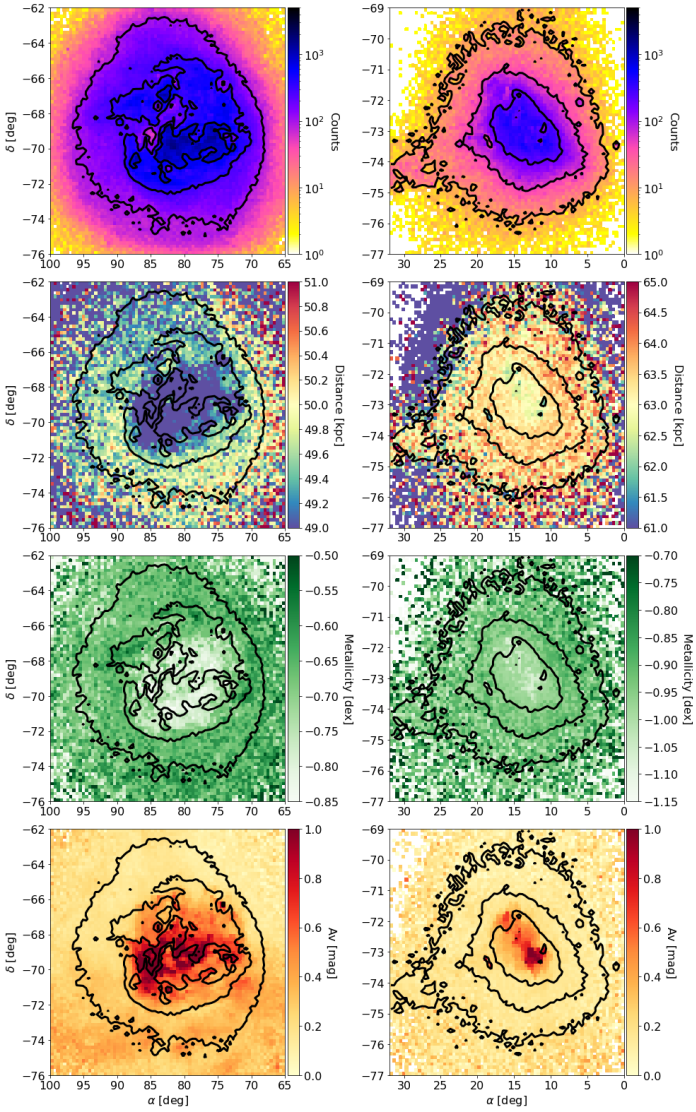

Fig. 9. Median sky density, distance, metallicity, and extinction maps (*from top to bottom*) of the Magellanic Clouds as seen by `StarHorse` (in equatorial coordinates and only including objects with `dist50` > 25 kpc). *Left panels*: centred on the LMC, *right panels*: on the SMC. The contour lines in each of the panels are derived from the sky density plots in the *top panels*. For the LMC, the contours are drawn at stellar densities of [100, 300, 700] per pixel (from outside inwards), with 905 205 sources within the outermost contour. For the SMC, the contour lines correspond to levels [10, 50, 200], with 195 634 sources contained inside the outermost contour.

4.5. Extinction maps

Figure 12 shows the median `StarHorse`-derived line-of-sight extinction per HealPix cell in four consecutive distance bins out to 2.5 kpc (from top to bottom), illustrating the gradual increase